frontiers | Frontiers in Earth Science

TYPE Original Research
PUBLISHED 23 September 2022
DOI 10.3389/feart.2022.1012085

OPEN ACCESS

EDITED BY
Duanyang Liu,
Chinese Academy of Meteorological Sciences, China

REVIEWED BY
Jianming Xu,
Shanghai Meteorological Bureau, China
Dai Zhujun,
China Meteorological Administration, China
Yong Huang,
Anhui Provincial Meteorological Bureau, China

*CORRESPONDENCE
Wei Xia-lu,
526098803@qq.com

SPECIALTY SECTION
This article was submitted to Atmospheric Science, a section of the journal Frontiers in Earth Science

RECEIVED 05 August 2022
ACCEPTED 02 September 2022
PUBLISHED 23 September 2022

CITATION
Cheng-gang W, Xia-lu W, Jia-de Y and Ting N (2022), Observational study of the influences of thermal and dynamic boundary layer on the vertical distribution of black carbon aerosol in ShouXian county in wintertime, 2016. *Front. Earth Sci.* 10:1012085. doi: 10.3389/feart.2022.1012085

Observational study of the influences of thermal and dynamic boundary layer on the vertical distribution of black carbon aerosol in ShouXian county in wintertime, 2016

Wang Cheng-gang[1], Wei Xia-lu[2]*, Yang Jia-de[1] and Ni Ting[3]

[1]Nanjing University of Information Science and Technology School of Atmospheric Physics, Nanjing, China, [2]Fujian Meteorological Information Center, Fuzhou, China, [3]ShouXian National Climate Observatory, Huaihe River Basin Typical Farmland Eco-Meteorology Field Scientific Experiment Base of China Meteorological Administration, Xian, China

Using vertical observation data of black carbon aerosol and meteorological parameters in the ShouXian area of Anhui Province from 14 December 2016 to 3 January 2017, the thermal and dynamic effects of the boundary layer on the vertical distribution structure of black carbon were studied. The results show that 1) of 82 vertical sounding profiles obtained during the observation period, there were 72 boundary layer sounding profiles dominated by heat and 10 profiles dominated by dynamics. 2) When thermal effects were dominant, the concentration of black carbon aerosol was significantly affected by diurnal changes in the boundary layer. In the unstable boundary layer, black carbon aerosol was uniformly distributed in the vertical direction; during the transition from an unstable to a stable boundary layer, the concentrations of black carbon aerosol were significantly higher in the lower layer than in the upper layer; in the stable boundary layer, the concentrations of black carbon aerosol decreased continuously with height; and during the transition from a stable to an unstable boundary layer, the black carbon aerosol concentrations exhibited high values in the upper layer, with the concentration difference reaching 4 μg m^{-3}. 3) When the dynamic effect was dominant, the structure of the vertical distribution of black carbon aerosol was affected by wind and by diurnal changes in the boundary layer simultaneously. The high winds (>4 m/s) removed the black carbon aerosol. In the unstable boundary layer, the black carbon aerosol uniformly distributed in the vertical direction had significantly lower concentrations in the high-wind range; when stable boundary layers occurred and during transitions from stable to unstable boundary layers, the black carbon aerosol concentrations were higher in the lower layer and lower in the upper layer. The stratification was more obvious than that observed under thermal control.

KEYWORDS

black carbon, vertical observation of boundary layer, thermal effect, dynamic effect, shouxian

Introduction

Black carbon (BC) aerosols not only pose a great threat to human health (Zhang et al., 2007), but also play an important role in environmental pollution, climate change, and extreme weather occurrences (Raunemaa et al., 1994; Ramanathan et al., 2002; Ramanathan and Carmichael 2008; Wang Y. et al., 2018a; Slater et al., 2021; Xiao et al., 2011).

The analysis of observational data is a direct means of understanding the spatial and temporal distributions of BC aerosol. Since the 1970s, a series of field observation experiments have been carried out in the United States (Waggoner and Charlson, 1976; Countess et al., 1980; Cass et al., 1982; Wolff et al., 1982), the United Kingdom (Singh et al., 2018), Switzerland (Herich et al., 2011), Finland (Pakkanen et al., 2000), and China (Luan and Mao, 1987; Tang et al., 1999; Weng et al., 2001; Zhang et al., 2015; Lu et al., 2015), leading to an in-depth understanding of the spatial and temporal distribution characteristics, source resolution and formation mechanisms of BC aerosol. However, these works are mostly based on near-surface analyses.

An increasing number of studies have indicated that the vertical distribution characteristics of BC aerosol have important effects on both atmospheric radiative forcing and physical processes in the boundary layer (Corrigan et al., 2008; Ramanathan and Carmichael, 2008; Li et al., 2015; Zhao et al., 2019; Zhang et al., 2015; Ding et al). Gordon (1997) and Duforet et al. (2007) showed that the absorptive heating of BC aerosols by shortwave radiation depends on their vertical distribution characteristics. Slater et al. (2021) used models to quantify this effect. When BC aerosol is concentrated at the top of the boundary layer, a "dome effect" is formed. That is, BC aerosol absorbs shortwave radiation at the top of the boundary layer and heats up the surrounding atmosphere, leading to a decrease in the turbulence intensity and inhibiting the development of the boundary layer, thus increasing ground pollution (Tian et al., 1997; Ding A. J. et al., 2016b; Huang et al., 2018; Y. Wang et al., 2018a; Z. Wang et al., 2018b; Liu et al., 2019; Zhao et al., 2020). At the same time, the cloud condensation nuclei (CCN) capability of BC is significantly enhanced (Ding AJ. et al., 2016a), which further affects indirect radiation. When BC aerosol is concentrated near the ground, its heating effect will, in turn, enhance turbulent motion and promote the development of an unstable boundary layer (Petj et al., 2016; Tian et al., 2019).

Li and Liang et al. (Li et al., 2015; Liang et al., 2016) found that the vertical structure of BC aerosol concentrations differed significantly throughout the day using outfield experimental data. Under stable conditions, BC aerosol concentrations were found to be significantly higher in the lower layers than in the upper layers (Zhang et al., 2012). The shallower boundary layer and temperature inversion layer increase the mass concentration of BC (Zhao et al., 2020). Under unstable conditions, the vertical distribution of BC aerosol is relatively uniform (Lu et al., 2019). When the wind speed is high, ground transport may either remove or exacerbate pollution, depending on the level of pollution in the upstream atmosphere (Zhao et al., 2020). In addition, BC aerosol concentrations are also influenced by the combination of the turbulent motion, temperature stratification, and wind field characteristics in the boundary layer. That is, physical processes in the boundary layer play important roles in the vertical distribution of BC aerosol.

At present, there are many individual case studies on the vertical distribution of BC aerosol (Altstdter et al., 2019; Lu et al., 2019). Zhao et al. (2019) and Shi et al. (2020) found BC aerosol through observations. Zhao et al. (2019) and Shi et al. (2020) found that the vertical structure of BC aerosol is strongly affected by local meteorological conditions, local pollution sources, land types, and atmospheric thermal and dynamic effects. However, when most studies are only 3–5 days, this article has been observed for 21 days and obtained 82 usable profiles. What's more, there are the profiles under different stability conditions, which is more representative.

Table 1 lists a series of vertical sounding measurements conducted by researchers in China in recent years. Through comparison, these studies mainly discuss the physical characteristics of BC aerosols and their effects on radiation, and lack the influence of boundary layer physical processes on BC profile. However, the distribution of BC mass concentration in the boundary layer is strongly affected by the thermal and dynamic effects of the atmosphere, so research in this area is indispensable.

With this foundation as a starting point, ground-based observations and vertical observations of the boundary layer in ShouXian County, Anhui Province, in winter 2016 were used, among other data, to compare and analyze the effects of dynamic and thermal processes within the atmospheric boundary layer on the vertical distribution characteristics of BC aerosol under different stability conditions.

Experiment

Observation experiment

To understand in detail the variation characteristics of the vertical structure of BC aerosol in a typical rural area in eastern China, Nanjing University of Information Science and

TABLE 1 Comparison of research contents of BC vertical sounding in different regions of China.

Observation area	Observation time	Observation height	Research content	References
Shouxian	14.12.2016-03.01.2017	0–1000 m	Thermal and dynamic effects of boundary layer on the vertical distribution of BC	This article
Beijing	25.11.2018-27.11.2018	0–3000 m	Physical properties of BC vertical profile during heavy pollution and its effect on radiation	Zhao et al., 2020
Beijing	late spring and winter	500–2500 m	Physical characteristics and parameterization of tropospheric vertical BC discuss the influence of BC on radiation	Zhao et al., 2019
Beijing and Europe	Beijing: 09.04-2018; 12.11-2018 Europe: 09.04-2008; 12.11-2008	0–10000 m	The physical properties related to the particle size of BC. The relationship between BC and CCN, radiation is discussed	Ding et al., 2016b
Xuzhou	13.07.2018-15.07.2018	0–3000 m	The effect of BC on radiation	Liu et al., 2019
Nanjing	2016-2019	0–1000 m	BC profile classification. Assess the effect of BC on radiative forcing and heating rate	Shi et al., 2020

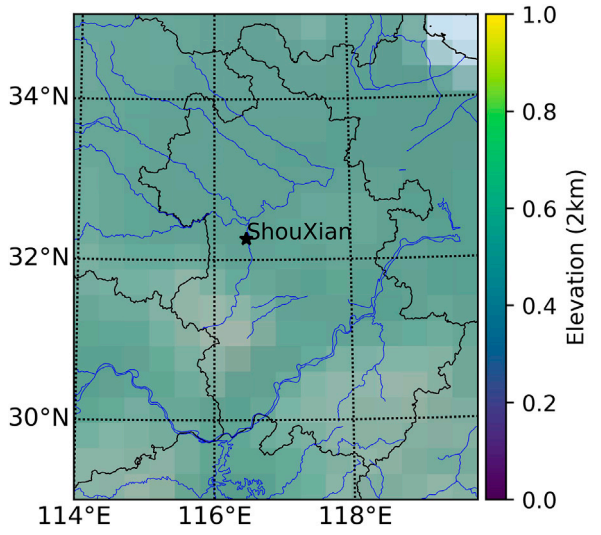

FIGURE 1
The location of the observation point. The black asterisk in the figure refers to ShouXian.

Technology (NUIST), together with Anhui Institute of Meteorological Science, conducted a 21-days comprehensive atmospheric boundary layer observation experiment in ShouXian County, Anhui Province, China, from 14 December 2016 to 3 January 2017. The observation site was the ShouXian National Climate Observatory (116.47E, 32.26N), the specific position is shown in Figure 1, located 9 km from the county, with flat surrounding terrain, homogeneous farmland in the subsurface, and no obvious pollution sources (Yang et al., 2017; Wang et al., 2020).

This experiment focused on the simultaneous observations of the three-dimensional structure of BC aerosol, PM2.5 and meteorological parameters. The ground observation instruments included a microAeth® AE-33 micro-aethalometer (Maggee, United States), a CAWSD600 automatic weather station (Huayun Technology Development, China), and a GRIMM180 particulate matter concentration monitor (GRIMM, Germany). The sampling frequency is 0.02HZ.

The vertical observation system mainly included a tethered balloon (XLS-II type, volume 5.25 m3; payload 5 kg, Supplementary Figure S1), a meteorological sensor (Institute of Atmospheric Physics, Chinese Academy of Sciences, Supplementary Figure S1) and a microAeth® AE-51 micro-aethalometer (Maggee, United States). Vertical observations were conducted eight times a day at 02, 05, 08, 11, 14, 17, 20, and 23 h (local time, local time = UTC + 8, same below). The collection frequency of meteorological data is 1HZ, while the collection frequency of BC and PM2.5 data is 0.2HZ. Due to the observation condition limitations, the observations were suspended when the wind speed was high (>7 m/s) or when precipitation occurred, so there were missing data in the later analysis.

The balloon ascent/descent rate (approximately 0.8 m/s) was controlled by an electric winch. Considering that the fish-shaped balloon was well balanced, the air flow disturbance was largely reduced during launch. Together with consideration of the timing accuracy of the observations, the ascent was chosen for the subsequent analysis.

Data processing

AE-51 has a measuring range of 0–1 mg m−3, a resolution of 1 ng m−3, an accuracy of 5%, and a sensitivity of < 0.1 μg m−3. The collected data were processed using the optimized noise-reduction averaging (ONA) algorithm (Hagler et al., 2011), and the light attenuation (ATN) of the averaging time window increments was determined by the internal filter of the instrument, reducing the light attenuation of the instrument(ΔATN), which in turn reduces the effect of instrument noise on the data. This expression is shown in Eq. 1 as follows:

$$BC_i = \frac{A_s}{Q \cdot E_{atn}} \times \frac{\Delta ATN_i}{\Delta t_i} \quad (1)$$

Where BC_i is the average mass concentration of black carbon (BC) aerosol in the i-th time interval (μg m−3);A_s is the sampling point area (7.1×10−6 m2); Q is the sampling flow rate (100 ml min−1);Δt_i is the sampling time interval (10s); andE_{atn} is the sampling time interval whenΔt_i is the effective mass absorption rate within the sampling interval.

AE-33 has an accuracy of 5% and a sensitivity of < 0.1 μg m−3. The dynamic zero-point test was performed at 00: 00 h in January of each month, and each test lasted for 20 min with a time resolution of 1 s. The average BC value of the zero-point test in this study was 0.01 ± 0.09 μg m−3; the BC values showed a normal distribution, and the expected value was 0.01 after fitting with the Gaussian distribution function, indicating that the instrument we used performed well during the observation period.

The data were measured using a dual-point measurement method (Virkkula et al., 2007; Cheng et al., 2018), and the BC aerosol mass concentration was calculated from the optical attenuation (ATN1 and ATN2) caused by two sampling points with different loading levels, as shown in Eqs 2, 3:

$$BC1_{raw} = BC_{zero\,loading} \times (1 - k \times ATN1) \quad (2)$$

$$BC2_{raw} = BC_{zero\,loading} \times (1 - k \times ATN2) \quad (3)$$

where BC1raw and BC2raw are the mass concentrations of BC aerosol at different flow rates through the sampling point (μg m−3), and BCzero loading is the revised value after removing the loading effect (μg m−3).

Considering that BC aerosol data measurements are affected by temperature, with the measured BC aerosol decreasing by 0.25 μg-m−3 for every 1°C increase in temperature within the sensor (Altstdter et al., 2019), this paper also applies a temperature revision to the BC data. Before the study, we verified the data quality of AE-33 and AE-51, see the attachment for details.

In addition, the sampling frequency of the meteorological data was 1 s/group. The collection frequency of AE-51 was 10 s/group. To eliminate mismatches between the meteorological data and BC data in the vertical direction, a 60-s averaging was performed for both datasets during the data processing. At the same time, unreasonable data from instrument malfunction or human factors were excluded. Variance tests, extreme value tests, and continuity tests were applied to control the quality of all observations and ensure data reliability and accuracy (Ren et al., 2015). The wind direction is divided into 16 directions, e.g., 348.75–360° and 0–11.25° are recorded as due north. 60-s mean wind direction is the most frequent wind direction occurring in the time frame.

In addition to the barometric pressure (P), temperature (T), relative humidity (RH), wind speed (WS) and wind direction (WD) data collected by the meteorological sensors, the atmospheric stability was calculated using the virtual potential temperature (VPT). For the calculation of VPT, see Eq. 4 (Wang, 1987) below:

$$VPT = T \times \left(\frac{P_0}{P}\right)^{\frac{R_d}{C_{pd}}} \left(1 + 6.08 \times 10^4 \left(\varepsilon \times \frac{e}{P - (1-\varepsilon)e} \times 1000\right)\right) \quad (4)$$

Where T is the measured air temperature (K);P andP_0 are the measured air pressure (hPa) and standard sea level pressure (hPa), respectively;R_d is the specific gas constant of dry air (287 J kg−1 K−1); C_{pd} is the specific heat capacity of dry air at a constant pressure and standard temperature (1005 J kg−1 K−1); ε is the mass ratio of water vapor molecules in air to dry air (0.622); and e is the water vapor pressure (hPa), which is the product of the saturation water vapor pressure at a given temperature (T) and relative humidity (RH).

The time series of ground pollutant concentrations and meteorological parameters during the observation period are shown in Figure 2. The solid lines and dotted lines in Figure 2A are the daily variations of BC aerosol and PM2.5, respectively. The solid lines and bars in Figure 2B are the relative humidity and precipitation, respectively. The solid line and arrows show the temperature and wind distribution respectively in Figure 2C, where the length of the arrow indicates the wind speed magnitude. During this period, the atmospheric circulation situation in the ShouXian area was relatively stable, with mainly cloudy weather, low surface wind speeds, high relative humidity, and small amounts of precipitation on 19-21 and 25-26 December. Under the influence of meteorological conditions, the BC aerosol and PM2.5 concentration trends were consistent, and there were 2 complete heavy pollution formation-dissipation processes (PM2.5 ≥ 150 μg m−3) during this period. That is, the first heavy pollution process on 18-20 December 2016, after which pollutants were rapidly cleared on the 21st under continuous precipitation flushing. The second heavy pollution process on 1–2 January 2017. After 13:00 on 2 January, the concentration of BC began to decrease, which was due to the elevation of the

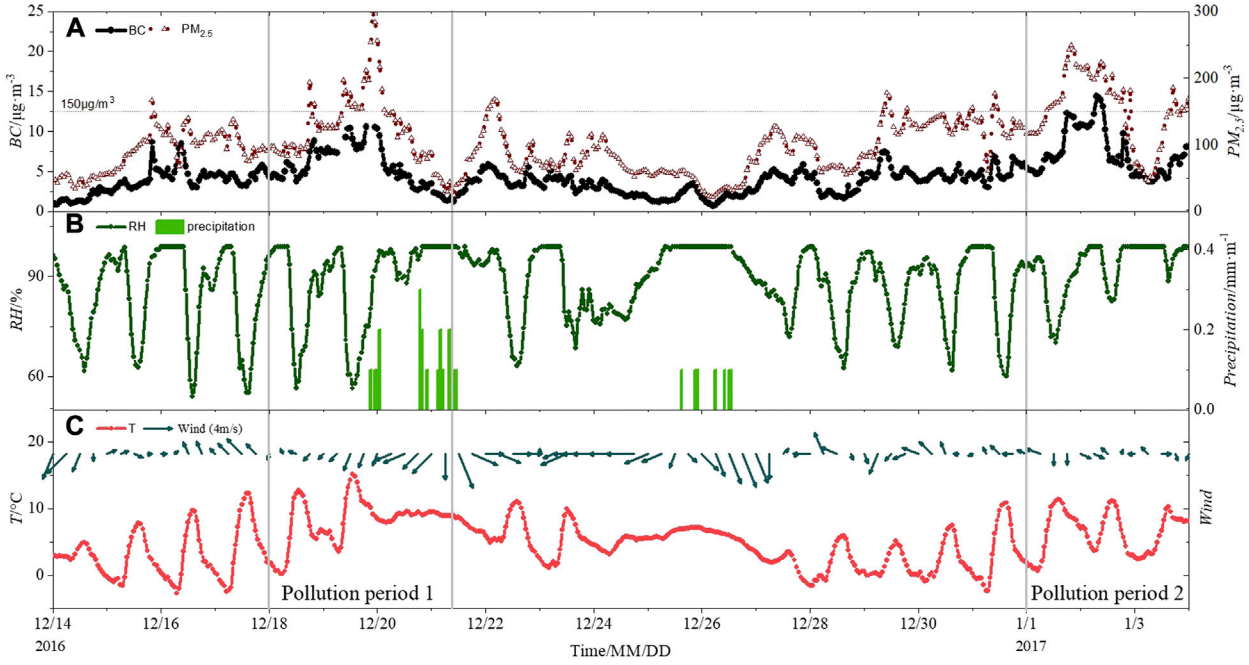

FIGURE 2
From 14 December2016 to 3 January 2017: the changes in ground pollutants and meteorological parameters over time **(A)** BC aerosol, $PM_{2.5}$; **(B)** relative humidity, precipitation; **(C)** temperature, wind).

boundary layer with the increase of solar radiation. The strong turbulent mixing effect caused BC to mix in the boundary layer, and combined with the clearing effect of high wind (Figure 10), the surface concentration decreased. After that, with the decrease of solar radiation and human activities, the pollutants gradually increased until the precipitation on the 4th (see Supplementary Figure S5 in the attachment), and the pollutants were removed.

Results and discussion

The atmospheric boundary layer structure has distinctive daily variation in its distribution characteristics due to the sunrise and sunset (Stull, 1988, See Supplementary Figures S3, S4 in the appendix). The boundary layer evolution process can be roughly divided into four periods according to differences in the vertical structure of the boundary layer: the unstable boundary layer period in the daytime, the unstable-to-stable boundary layer transition period in the evening (referred to as transition period 1), the stable boundary layer period at night, and the stable-to-unstable boundary layer transition period (transition period 2). Location of the maximum vertical gradient of virtual potential temperature was used to determine the height of the boundary layer by calculating the virtual potential temperature profile based on the temperature, humidity and wind speed profiles observed by the sounding. According to the Richardson number, the atmospheric stability is judged; the virtual potential temperature profile is compared with the typical profile (not shown here) of Stull (1988) to finally determine the boundary layer structure and type.

Atmospheric stability varies highly in the boundary layer at different times of the day. The ability of turbulence to disperse pollutants vertically varies, depending on the stability. Atmospheric stability also directly affects the vertical and horizontal transport of pollutants by changing the thermal and dynamic effects in the boundary layer. At this stage, the Richardson number (R_f) is used to determine the atmospheric stability (Vogelezang and Holslag, 1996; Seidel et al., 2012; Guo et al., 2016).R_f is defined as the ratio of buoyancy-related turbulence to mechanical shear-induced turbulence; when$R_f < 1$, the system is dynamically unstable, and when$R_f > 1$, the dynamics are stable (Stull, 1988). Due to the discontinuity of the observed height, the overall Richardson number is commonly used in practical calculations (R_B, Eq. 5). The Richardson number can be calculated as follows:

$$R_B = \frac{g\Delta\overline{VPT}\Delta Z}{\overline{VPT}(\Delta u)^2} \quad (5)$$

where g is the acceleration of gravity; VPT is the virtual potential temperature; Z is the height; and u is the horizontal wind speed. The data of two adjacent layers are used in the paper, and the Richardson number is calculated every 50 m.

TABLE 2 Profile statistics under different boundary layer conditions.

Boundary layer type	Total	Thermal effects dominate the profile	Dynamic effects dominate the profile
Unstable boundary layer	34	31	3
Transformation of unstable to stable boundary layer(Transition period 1)	8	8	0
Stable boundary layer	33	27	6
Transformation of stable to unstable boundary layer(Transition period 2)	7	6	1

In addition to atmospheric stability, wind speed is another important factor that affects the atmospheric dispersion capacity (Li, 1985). A study by Guiqin et al. (2016), Liu et al. (2002) and Sun et al. (2016) pointed out that wind speeds greater than 4 m/s in the boundary layer are favorable for pollutant dispersion. Therefore, in this paper, wind speeds (>4 m/s) and the vertical shear of horizontal wind speeds between two height layers (>1 m/s/50 m) are considered, with $R_B < 1$ as the judgment condition of the boundary layer dominated by dynamic action. The rest of the stability is attributed to the thermally controlled boundary layer.

Based on the above criteria, Table 2 counts the number of contour lines in each of the four boundary layers under the dominant dynamics and thermal controls. A comparative analysis showing the effects of dynamic and thermal processes within the atmospheric boundary layer on the vertical distribution characteristics of BC under different stability conditions was conducted. Due to the limitation of the tethered balloon sounding conditions, 82 effective profiles were obtained because observations could not be made under adverse weather conditions such as precipitation or high winds. Among the obtained cases, more cases were observed under unstable boundary layer and stable boundary layer conditions, with 34 and 33 cases, respectively; fewer cases were obtained for Transition 1 and Transition 2, with only 8 and 7 cases, respectively. Among all boundary layer types, the share of thermodynamic dominance was as high as 87.8%, especially in Transition1, where only thermodynamic dominance data were observed. The number of boundary layers dominated by dynamics was small, with a percentage of only 12.2%. However, previous studies have shown that wind plays an important role in the diffusion and three-dimensional transport of BC (Wang et al., 2001; Liu et al., 2002). Therefore, the influence of dynamics on variations in BC concentrations in the boundary layer cannot be ignored.

Figure 3 shows the vertical profile distribution of the average value of BC, temperature, virtual potential temperature, wind speed and wind direction obtained during the winter observation period. According to Figure 3A, the concentration of BC is the highest at the ground, about 11.01 μg m^{-3}, and decreases rapidly with height. The concentration of BC at 150 m decreases to 4.09 μg m^{-3}. In 150–800 m BC decreases only 2.20 μg m^{-3} with height. Above 800 m, the BC concentration remains unchanged. The short blue line is the standard deviation line, and the standard deviation also decreases with the height, indicating that the concentration of BC changes higher at the low altitude, but few at the high altitude. The temperature profile in Figure 3B shows that from the ground to 150 m, the inversion is weak to the ground, but in the position temperature profile (Figure 3C), the virtual potential temperature increases slowly with the height, indicating a weak stable stratification ($\partial VPT/\partial z$=0.77K/100 m), and the wind speed gradually increases from 1 m/s to 3.3 m/s. Under the superposition of stratification conditions and wind, the concentration of BC decreases with height.

Although the BC concentration is generally high on the ground and low in the upper air, the shape of the BC profile is different under different boundary layer conditions. The influence of dynamic and thermal conditions on the BC concentration under different boundary layer conditions will be discussed in detail below.

Influence of the thermal effects of the boundary layer on the vertical structure of black carbon

Figures 4–7 show the distributions of BC, temperature, virtual potential temperature, wind speed and wind direction over the vertical profile under the four boundary layer conditions. Among them, a-e are the vertical distribution maps of each element under unstable boundary layer conditions. In the evolution process of boundary layer, due to the influence of weather, advection and other factors, sometimes the imaginary virtual potential temperature profile of each stage is not exactly the same as the diurnal cycle evolution profile of boundary layer of Stull. Under normal conditions, thermal action is the main reason for the formation of an unstable boundary layer. In particular, turbulent activity is strong in boundary layers due to the thermal forcing of the surface at noon. The vertical distribution of meteorological parameters within a boundary layer is more uniform under the effect of turbulent mixing. The virtual potential temperature profiles at 11:00 and 14:00 on 18 December 2016 basically meet the conditions that $\partial VPT/\partial z < 0$ near the ground and $\partial VPT/\partial z \approx 0$ in the middle and

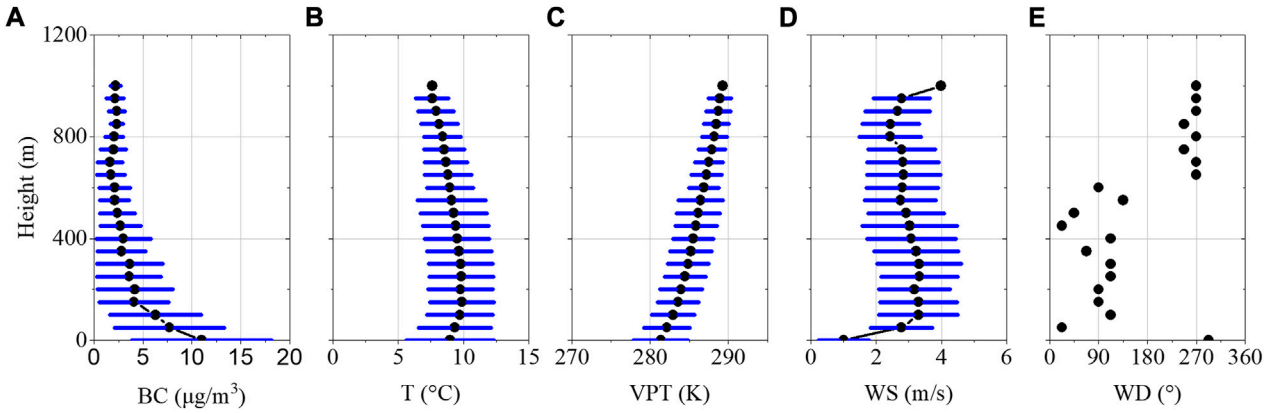

FIGURE 3
During winter observation period, BC, T, VPT, WS and WD contours. Blue lines are BC standard deviation line. **(A)** black carbon aerosol vertical profile, **(B)** temperature vertical profile, **(C)** virtual potential temperature vertical profile, **(D)** wind speed vertical profile, **(E)** wind direction vertical profile.

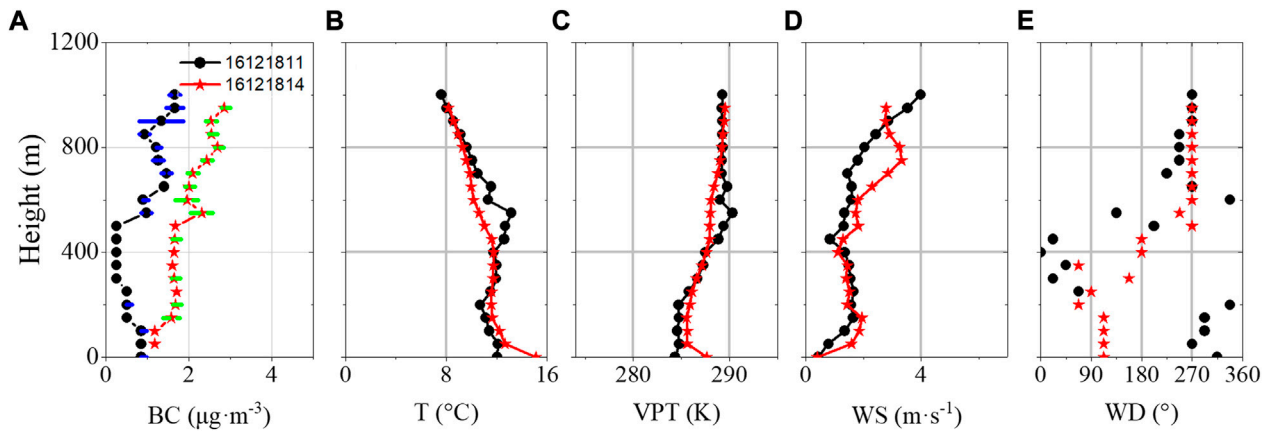

FIGURE 4
Thermally controlled unstable boundary layer BC, T, VPT, WS and WD contours. The black line indicates the contours of each element at 2016121811 and the red line indicates the contours of each element at 2016121814. Green and blue lines are BC error bars. **(A)** black carbon aerosol vertical profile, **(B)** temperature vertical profile, **(C)** virtual potential temperature vertical profile, **(D)** wind speed vertical profile, **(E)** wind direction vertical profile.

upper layers. In this paper, two times were used as typical individual cases among many samples for analysis. As seen in Figure 4A, the BC concentrations throughout the vertical profile (black dotted lines) at 11:00 on 18 December 2016 have slight differences among the three altitude ranges. The profiles below 200 m and above 550 m have large concentration values, 0.86 μg m^{-3} and 1.95 μg m^{-3}, respectively. Figure 4B and Figure 4C show the vertical profiles of temperature and virtual potential temperature. The temperature profile at the moment shown in the Figure indicates an overall decreasing trend, with a hanging inversion (intensity of 0.66°C/100 m) in the range of 200–550 m. The corresponding virtual potential temperature profile also shows a strong stable structure. The wind speed below 700 m (Figure 4D) is less than 1.5 m/s, and the wind direction (Figure 4E) is variable. In summary, the height of the mixed layer is approximately 200 m. The turbulent transport effect is strong, and horizontal transport is weak in the mixed layer. BC is more uniformly distributed in the lower layer, 200–550 m, and due to the existence of top inversion, turbulent mixing is suppressed. The vertical transport of BC is blocked and BC cannot enter the inversion layer, so the BC concentration is lower in this height interval.

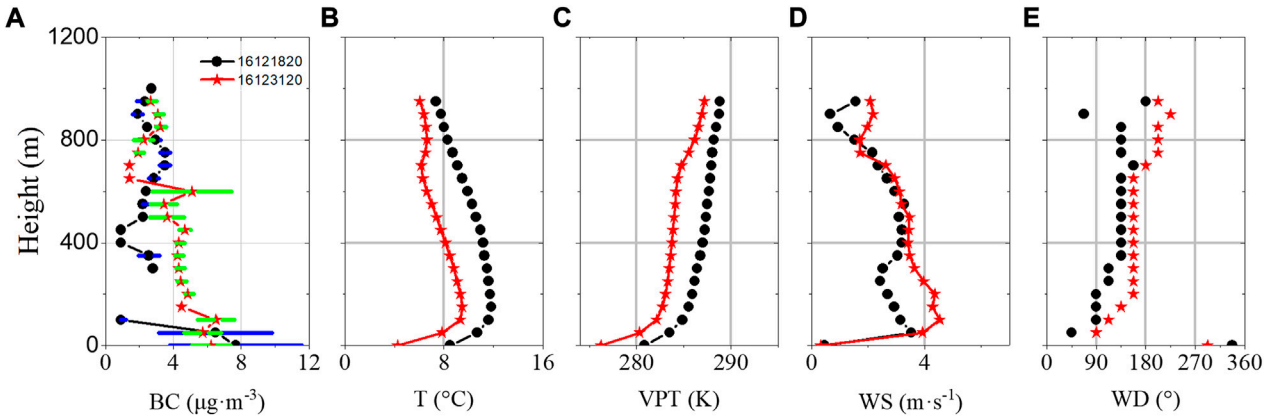

FIGURE 5
Thermally controlled transformation of unstable to stable boundary BC, T, VPT, WS and WD contours. The black line indicates the contours of each element at 2016121820 and the red line indicates the contours of each element at 2016123120. Green and blue lines are BC error bars. **(A)** black carbon aerosol vertical profile, **(B)** temperature vertical profile, **(C)** virtual potential temperature vertical profile, **(D)** wind speed vertical profile, **(E)** wind direction vertical profile.

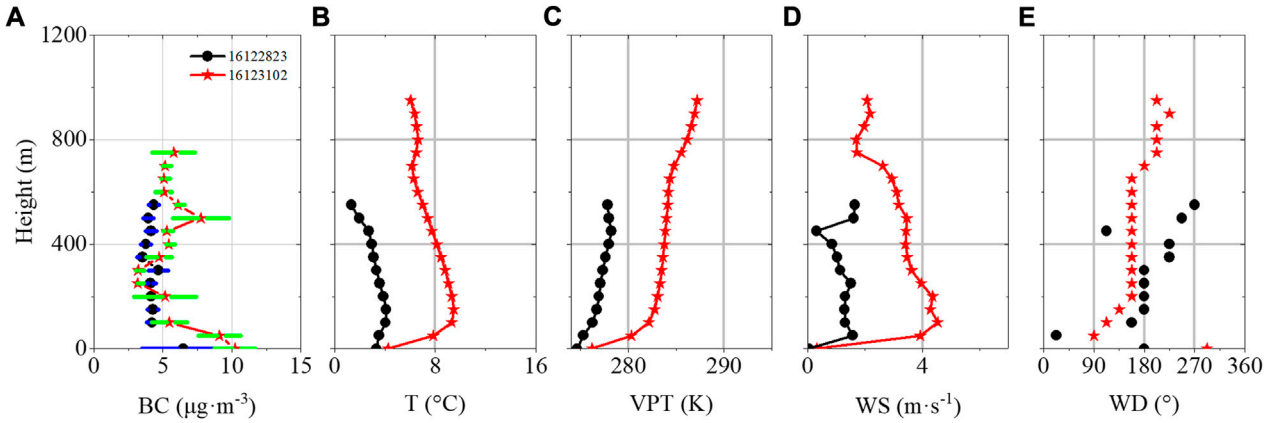

FIGURE 6
Thermally controlled stable boundary BC, T, VPT, WS and WD contours. The black line indicates the contours of each element at 2016122823 and the red line indicates the contours of each element at 2016122302. Green and blue lines are BC error bars. **(A)** black carbon aerosol vertical profile, **(B)** temperature vertical profile, **(C)** virtual potential temperature vertical profile, **(D)** wind speed vertical profile, **(E)** wind direction vertical profile.

The thermal effect is more obvious at 14:00 than at 11:00 on 18 December 2016. As seen in the figure, the suspended inversion disappears at 200 m. Turbulent activity within the mixed layer is stronger at this time than at other times. The vertical distribution of BC (red dotted line) is more uniform, with an average concentration of 2.19 μg m^{-3}. From the ground to a height of 50 m is a superadiabatic layer with a decreasing temperature rate of up to 4.85°C/100 m. The layer junction is in a strongly unstable state ($\partial VPT/\partial z = -4.11K/100m$). The vertical wind speed profile is similar to that seen at 11:00, with a slight shift in the wind direction. Therefore, in such a boundary layer, the layer junction is extremely unstable. Turbulent activity caused by the thermal effect is strong. Convection in the vertical direction is strong. The influence of the dynamic effect on BC remains small, and BC is uniformly mixed in the vertical direction with concentration fluctuations <0.5 μg m^{-3}.

Figure 5A–E shows the structures of the vertical distributions of the parameters during transition 1. In the evening, surface radiation cools as solar radiation disappears. Ground inversion occurs, with the lower layers showing stable boundary layer

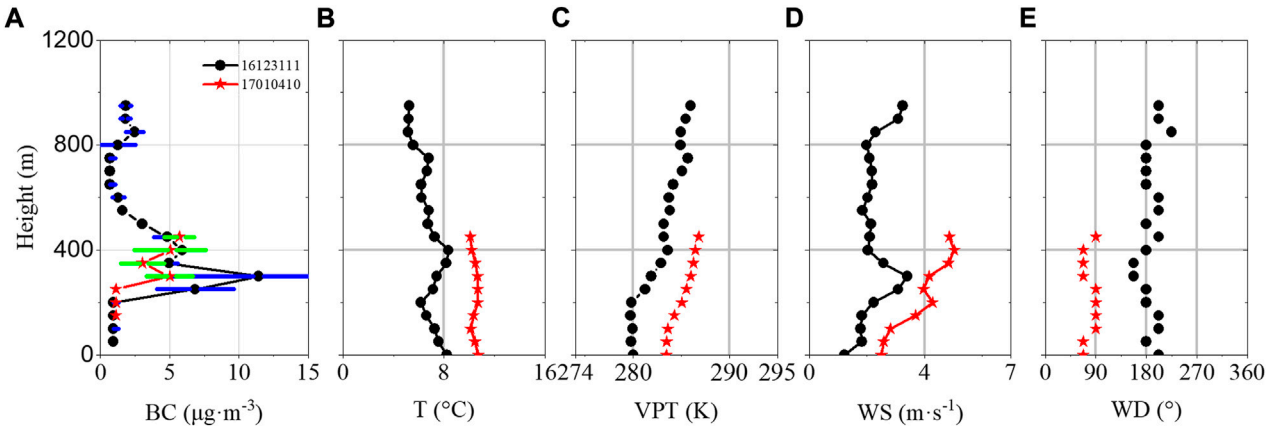

FIGURE 7
Thermally controlled transformation of stable to unstable boundary BC, T, VPT, WS and WD contours. The black line indicates the contours of each element at 2016122311 and the red line indicates the contours of each element at 2017010410. Green and blue lines are BC error bars. **(A)** black carbon aerosol vertical profile, **(B)** temperature vertical profile, **(C)** virtual potential temperature vertical profile, **(D)** wind speed vertical profile, **(E)** wind direction vertical profile.

characteristics, and pollutants decrease with height. The upper layers retaining unstable boundary layer characteristics from the previous moment, the vertical distribution of pollutants is relatively uniform. The temperature profiles of 20:00 on 18 December 2016 and 20:00 on 31 December 2016 are the closest to the standard profile, so they are analyzed as typical cases in this period. From the BC concentration profile obtained at 20:00 on the 18th (Figure 5A; black dotted line), it can be seen that the concentration of BC in the lower layer is significantly larger than that in the upper layer. The near-surface mean concentration is approximately 7.7 μg m^{-3}, which decreases rapidly with increasing height (BC data are missing at 150–250 m). The BC concentration above 300 m is approximately 2.3 μg m^{-3}. In Figures 5A,B strong ground inversion occurs below 100 m, with an intensity of approximately 3.1°C/100 m. The virtual potential temperature profile also shows a strong stable structure (see Figure 5C). The temperature and virtual potential temperature profiles above 100 m are similar to those at 17:00 (omitted), which reflect the atmospheric characteristics of the upper layers retained at the peak of the mixed layer development after turbulence disappears. At 20:00, due to the weak vertical transport of turbulence in the ground inversion layer combined with the effect of evening peak motor vehicle emissions, BC in the near-earth layer cannot be transported upward, and the upper layers retain their concentrations from the previous time period. The BC concentrations in the lower layers are significantly larger than those in the upper layers.

The profiles of each element (red dotted lines) at 20:00 on the 31 December 2016 are similar to those seen at 20:00 on the 18th. Additionally, the characteristics of the two boundary layer types at the time of Transition 1 are shown. The BC profile is distributed in two segments. From the surface to 550 m, the BC concentration slowly decreases from 6.2 μg $m^{-3}$to 3.2 μg m^{-3}. Above 550 m, the average BC concentration is 1.9 μg m^{-3}. A strong ground inversion occurs below 100 m at this time, with an intensity of approximately 5.06°C/100 m. The virtual potential temperature profile also shows a strong stable structure. The temperature and temperature profiles above 100 m still retain the characteristics of the atmosphere at the peak mixed layer development. It can be seen from the above that during Transition 1, an inversion appears close to the ground, and the turbulence-induced vertical transport is weak. The BC concentration values decrease continuously with height inside the inversion layer. However, outside the inversion layer, the BC concentration is still characterized by an unstable boundary layer.

Figure 6A–E shows the structures of the vertical distributions of the parameters of stable boundary layers. The stratification is more stable here than Transition 1 due to continued radiative surface cooling, weak turbulent activity and increased ground inversion thickness, which often occurs from night to early morning. The near-ground ∂VPT/∂z>0 at 23:00 on 28 December and at 0:00 on 31 December 2016 is an obvious virtual temperature profile characteristic at the stable boundary. Therefore, this paper takes it as a typical case for analysis. During the high ground level BC concentrations seen at 23:00 on the 28th, ground level concentration was 6.5 μg m^{-3}. The data are missing for the layer from 50–100 m, and the concentrations above 100 m fluctuate around approximately 4.1 μg m^{-3}. In the temperature profile (Figure 6B), the inverted temperature is close to the

ground below 100 m, while the corresponding virtual potential temperature (Figure 6C) increases with height. The wind speed and direction (Figure 6D,E) have less effects on the BC concentration than does temperature. In the stable boundary layer, the turbulent vertical transport is weak. Near-surface BC cannot reach high altitudes, and high altitudes are still characterized by daytime mixed layers. The BC profile is clearly stratified.

At 02:00 on 31 December 2016, the stable boundary layer characteristics were still obvious. Due to the thermal effect, the BC profile could be divided into two segments. Below 200 m, the average BC concentration is larger than above, at approximately 9.3 μg m^{-3}. Above 200 m, the BC concentration fluctuates at approximately 3.0 μg m^{-3}. The ground inversion temperature ranges from 0 to 200 m, and the intensity is 1.36°C/100 m. The virtual potential temperature profile also shows a strong stable structure. The wind speed of the whole layer is less than 3 m/s. In summary, stable boundary layers where thermodynamic effects dominate often have strongly stable structures with inversion temperatures. The wind speed is small; the turbulence activity is weak; BC diffuses poorly in the vertical direction; and the profile shows a two-segment distribution of with the lower level characterized by high BC and the upper level characterized by low BC.

Figure 7A–E shows the vertical structure profile of each element during Transition 2. The stable boundary layer is transitioning to an unstable boundary layer, which often occurs during the morning hours. The surface is heated by the solar radiation that it receives. The thermal effect strengthens the turbulent activity, and the heat is transferred upward. The ground inversion in the lower part of the boundary layer disappears, while the upper part remains a stable layer junction. At 11:00 on 31 December 2016 and 10:00 on 4 January 2017, the virtual potential temperature profile satisfies the conditions that the near ground $\partial VPT/\partial z$ is slightly less than 0, the middle layer $\partial VPT/\partial z > 0$, and the upper layer $\partial VPT/\partial z \approx 0$, which is most similar to the standard profile. In this paper, we choose 11:00 on 31 December 2016 and 10:00 on 4 January 2017 as typical cases for analysis. The BC (Figure 7A) profile shows a nose-like structure at 11:00 on 31 December. The concentration remains at a constant value of 0.9 μg m-3 below 200 m. At heights of 200–300 m, the concentration of BC increases with height up to 11.4 μg m^{-3}, followed by reduced concentration at 300–500 m. Above500 m, the concentration fluctuates between 0.7 and 2.1 μg m^{-3}. The ground inversion (Figure 7B) disappears due to solar radiation, and an overhanging inversion develops at 200–400 m. The virtual potential temperature profile (Figure 7C) hardly varies with height below 200 m, and above 200 m, it shows a stable layer junction. The wind speed and direction (Figure 7D,E) indicate a small southerly wind. Because the wind speed at 400 m reached 7 m/s on 30 December (figure omitted), the wind direction was southerly, Hefei urban area transmitted a large number of pollutants to Shouxian. BC accumulates in the suspended inversion layer, where the turbulent activity inside the overhanging inversion layer is weak, and BC cannot be exchanged with the outside layers. The concentration is 5.2 μg m^{-3} higher inside than outside the inversion layer.

At 10:00 on 4 January 2017, the profile distribution of each element was similar to that at 11:00 on 31 December. The near-surface turbulent activity is strong, the ground inversion disappears and an unstable boundary layer appears. However, the turbulent activity aloft is weak, and there is an overhanging inversion at heights of 100–250 m. The decreasing rate of the virtual potential temperature below 100 m ($\partial VPT/\partial z$=0.15 K/100 m) is less than the increasing rate of the upper level ($\partial VPT/\partial z$=0.85 K/100 m). Under this layer condition, the BC profile is divided into two segments. At 150 m–250 m, there is a constant BC concentration of 0.9 μg m^{-3}. At 250 m–450 m, the concentration increases to 5.4 μg m^{-3}. During the transition from a stable to unstable boundary layer, the ground inversion disappears. However, the upper layers still retain its inversion structure. When the stable boundary layer changes to the unstable boundary layer, the ground-level inversion disappears, but the inversion structure still remains in the upper layer. Weak turbulent transport makes it impossible for black carbon to break through the bottom of the suspended inversion layer, resulting in the difference of BC concentration inside and outside the inversion layer.

Sometimes, in the unstable boundary layer, the ground is superadiabatic, and turbulent activity caused by thermal effects is strong. Under these conditions, BC is mixed uniformly in the vertical direction, and the fluctuation range of the concentration is less than 2.5 μg m^{-3}. In Transition 1, a ground inversion of temperature appears. The turbulence-induced vertical transport capacity is weak. The BC concentration decreases continuously with height. The intensity of the ground inversion in the stable boundary layer strengthens continuously with time, and BC accumulates near the ground. In Transition 2, due to the emergence of solar radiation, the near-surface turbulence activity is enhanced. The ground inversion disappears, but the upper layers still retain their inversion structure. The BC profile is split by the overhanging inversion, and high BC concentrations appear in the upper layers, with concentration differences up to 4 μg m^{-3}.

Effect of boundary layer dynamics on the vertical structure of black carbon

From January 1st to 2 January 2017, the surface $PM_{2.5}$ increased rapidly from 116.42 μg m^{-3} to 227.65 μg m^{-3} from 04:00 to 18:00 on 1 January. From 16:00 on 1 January to 13:00 on 2 January, surface $PM_{2.5}$ fluctuated at 214.25 μg m^{-3}. After 13:00 on 2 January, $PM_{2.5}$ concentration began to decrease. The diurnal variation of air temperature decreased with the increase

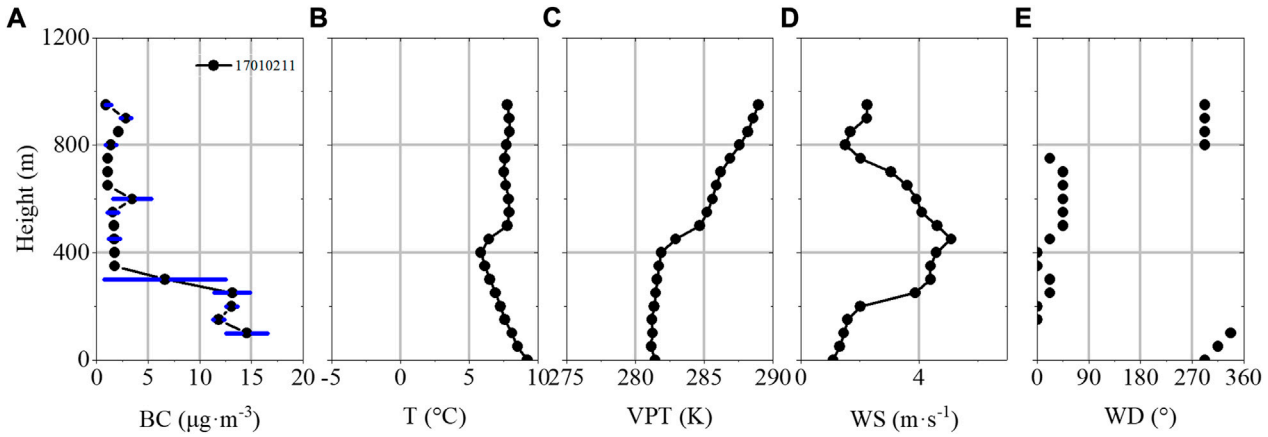

FIGURE 8
Dynamic controlled unstable boundary BC, T, VPT, WS and WD contours. The black line indicates the contours of each element at 2017010211. Blue lines are BC error bars. **(A)** black carbon aerosol vertical profile, **(B)** temperature vertical profile, **(C)** virtual potential temperature vertical profile, **(D)** wind speed vertical profile, **(E)** wind direction vertical profile.

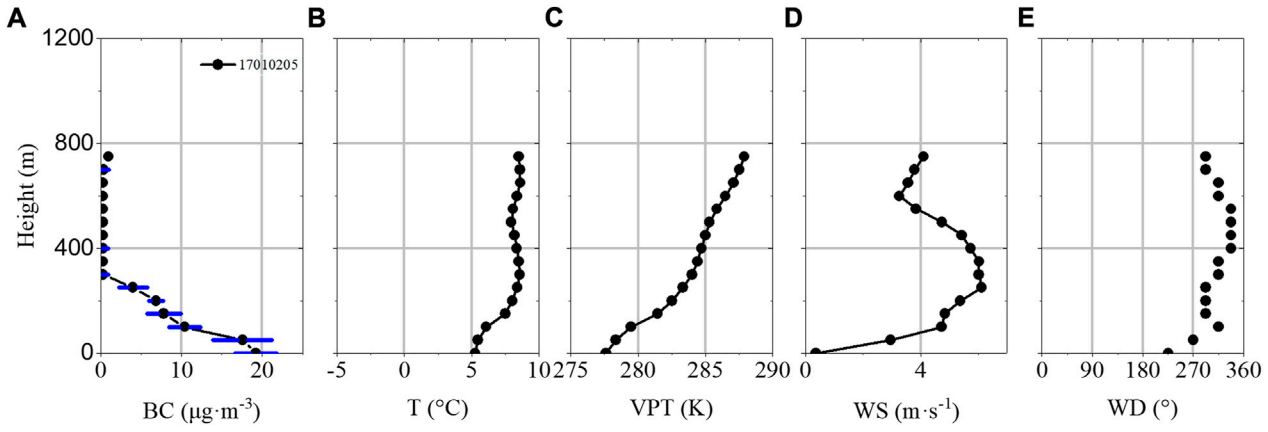

FIGURE 9
Dynamic controlled stable boundary BC, T, VPT, WS and WD contours. The black line indicates the contours of each element at 2017010205. Blue lines are black carbon error bars. **(A)** black carbon aerosol vertical profile, **(B)** temperature vertical profile, **(C)** virtual potential temperature vertical profile, **(D)** wind speed vertical profile, **(E)** wind direction vertical profile.

of $PM_{2.5}$ concentration, and the relative humidity was always above 70%. The surface wind speed is between 0.35 m/s and 2.95 m/s, and the dominant wind direction is north and northwest. There is weak northerly wind pollution transport. Meanwhile, the track 24 h after 00:00 on 2 January, (Supplementary Figure S6), also shows that there is weak northerly wind cold transport.

The selection of typical profiles under different boundary layer conditions when the dynamic action is dominant is consistent with that when the thermal effect is dominant. The time when the temperature profile is most similar to the standard profile is selected as a typical case. Figures 8–10 the vertical profiles of BC, temperature, virtual potential temperature, wind speed and wind direction for different boundary layer conditions when the dynamic effects dominate. Only three boundary layer types are available due to the lack of data for Transition 1, when dynamic effects dominate. At 11:00 on 2 January 2017, the dynamically controlled unstable boundary layer (Figure 8A–E) is characterized by some similarities to the thermally controlled layer, such as high turbulent activity. However, when high wind speeds occur, high winds have a powerful transport effect on material at the corresponding heights. As seen in Figure 8A, below 200 m, the BC concentration is high, approximately 12.9 μg m^{-3}. Then, it decreases slowly with height to

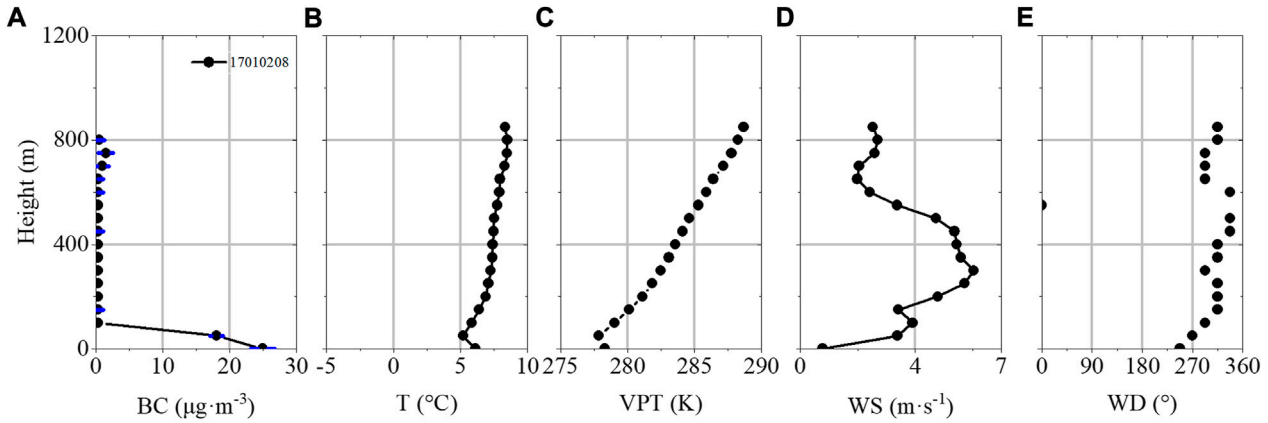

FIGURE 10
Dynamic controlled transformation of stable to unstable boundary BC, T, VPT, WS and WD contours. The black line indicates the contours of each element at 2017010208. Blue lines are BC error bars. **(A)** black carbon aerosol vertical profile, **(B)** temperature vertical profile, **(C)** virtual potential temperature vertical profile, **(D)** wind speed vertical profile, **(E)** wind direction vertical profile.

1.2 μg m^{-3} at 350 m. Above 350 m, the concentration fluctuates at approximately 1.4 μg m^{-3}. Below 400 m, the temperature (Figure 8B) decreases with height, and the corresponding virtual potential temperature (Figure 8C) is almost constant. The wind speed (Figure 8D) has a nose-like structure in the profile. From 200–450 m, the wind speed increases rapidly from 2 m/s to 5 m/s. Above 450 m, the wind speed decreases with height. From the ground to an altitude of 700 m, westerly winds change clockwise to northerly winds (Figure 8E). In summary, when the wind speed is small, the characteristics of the thermally controlled boundary layer are more obvious. For instance, below 200 m, the turbulence activity is strong, and the BC concentration is uniformly distributed. As the wind speed increases, gales play a diffusion and removing role for BC. For example, above 200 m, the BC concentration decreases slowly with height.

Figure 9A–E show the vertical structure profiles for each element of stable boundary layers under dynamic control. In this paper, we choose 05:00 on 2 January 2017 as typical cases for analysis. BC (Figure 9A) has the highest concentration at the ground level, reaching 19 μg m^{-3}. From the ground to 300 m, BC decreases rapidly with height. Then fluctuating at approximately 0.3 μg m^{-3} above 300 m. In Figure 9B and Figure 9C, there is a ground inversion below 300 m with an intensity of approximately 1.11°C/100 m, exhibiting a strong stable structure (∂VPT/∂z = 2.12 K/100 m). The wind speed (Figure 9D) profile shows an obvious nose-like structure in the height range from 50–600 m. The maximum wind speeds appear at 300 m and 6 m/s, and the wind direction is northwest (Figure 9E). Above 300 m, the wind speed remains >4 m/s. It is thus clear that the wind speed is high in the whole layer, and the gusty wind plays a scavenging role on BC. The BC concentration decreases with height at the lower level (300 m) under the combined effect of the ground inversion and gusty winds. The BC concentration is still low at high altitudes due to high winds. Therefore, the BC profile shows a clear structure of low-level high concentrations and upper-level low concentrations.

During Transition 2 (Figure 10A–E, 08:00 on 2 January 2017), the unstable boundary layer starts to disappear due to solar radiation. The BC (Figure 10A) concentration is highest fluctuated around the surface (25.0 μg m^{-3}) and fluctuates at approximately 0.38 μg m^{-3} above 100 m. Turbulence activity is intense from 0–100 m, and the layer junction is extremely unstable (Figure 10B,C, ∂VPT/∂z = -0.92 K/100 m). The top inversion temperature remains above 100 m. The wind speed at 50–600 m (Figure 10D) is higher than 4 m/s, and the nose-like structure is obvious. The wind direction (Figure 10E) is a uniform northwest wind. During Transition 2, the BC concentration decreases rapidly at heights of 50–100 m due to the effect of the top cover inversion. Above 50 m, high winds can significant lower BC concentration. Therefore, the BC concentration is high in the lower layer and low in the upper layer, and the high and low air stratification is more obvious under these conditions than that under thermal control.

Clearly, under dynamically dominated boundary layer conditions, high winds play a diffuse removing role for BC, in agreement with Altstdter et al. (2019), Wei et al, (2020), Caputi et al., 2018, Miao et al., 2019, and others. However, due to the small amount of data in this study, there may still be some errors in the vertical profile distribution of BC in the actual winter boundary layer, and more data are needed to further validate definitive conclusions. In addition, due to the small amount of data used in this study, there may still be some errors within the vertical profile distribution of black carbon in the actual winter boundary layer. More data are needed to further verify this conclusion.

Conclusion

In this study, vertical observations of BC and meteorological parameters in the ShouXian County area during the winter of 2016 were used to analyze and discuss the influence of the thermal and dynamic characteristics of the boundary layer on the vertical distribution of BC. The results are as follows.

1) A total of 82 effective profiles were obtained during the observation period, with a small proportion, 12.2%, dominated by dynamic effects, and the rest representing boundary layer profiles dominated by thermal effects. Among the four boundary layer types, the unstable boundary layer and stable boundary layer appeared more frequently, 34 and 33 times, respectively; the occurrence numbers of Transition 1 and Transition 2 cases were 8 and 7, respectively.

2) When thermodynamics dominate, in the unstable boundary layer, turbulence activity is strong, convection in the vertical direction is strong, and BC is evenly distributed in the vertical direction. During Transition 1, the ground inversion temperature appears, and the turbulence activity is weak. The BC concentrations in the near-ground layer cannot be transported upward. The BC concentrations in the unstable boundary layer are retained in the upper layers, and the BC concentrations in the lower layers are significantly larger than those in the upper layers. In the stable boundary layer, the ground inversion is deeper than that in the unstable layer, and the layer junction is more stable. Under these conditions, turbulence activity is further suppressed, and the BC concentration decreases continuously with height. During Transition 2, an overhanging inversion appears, turbulence activity in the inversion layer is weaker, BC cannot be exchanged with the outside world, the profile is divided by the overhanging inversion, and the concentrations show high values in the upper layers.
3) The BC profiles are similar to that of the thermodynamically dominated profile when these dynamics are dominant. The BC concentrations are evenly distributed in regions of low wind speeds in unstable boundary layers and decrease significantly in regions of high wind speeds (>4 m/s). In stable boundary layers and during Transition 2, the wind removal effect is significant, the BC concentration is higher in the lower layer and lower in the upper layer, and stratification is more obvious than that observed under thermal control.

This study did not consider the influence of regional transport on the BC profile, and there are still many shortcomings. Meanwhile, BC has a strong absorption effect on solar shortwave radiation. If further studies confirm the relationship between BC aerosol profile distribution and boundary layer evolution, this paper can provide a profile reference for subsequent radiation simulations and can provide a feasible idea for air pollution control.

Data availability statement

The raw data supporting the conclusions of this article will be made available by the authors, without undue reservation.

Author contributions

WC-G and WX-L are responsible for data processing and thesis writing. YJ-D is responsible for observing instrument maintenance. NT is responsible for the observation test.

Funding

This study was supported by the National Natural Science Foundation of China (Grant 41975011).

Acknowledgments

We thank the ShouXian County National Climate Observatory for providing ground-level meteorological data and pollutant data and the hard-working teachers and students who conducted the observation experiments.

Conflict of interest

The authors declare that the research was conducted in the absence of any commercial or financial relationships that could be construed as a potential conflict of interest.

Publisher's note

Supplementary material

The Supplementary Material for this article can be found online at: https://www.frontiersin.org/articles/10.3389/feart.2022.1012085/full#supplementary-material

SUPPLEMENTARY FIGURE S1
A tethered balloon and a meteorological sensor. In this observation test, AE-33 micro-Aethalometer measured ground BC data and AE-51 measured high-altitude BC data. In order to verify the consistency of data quality measured by the two instruments, the two kinds of BC data are compared and verified in this paper. In the preparation stage for the moored motorboat to lift off, we turn on the AE-51 collector, so we have a period of time to measure on the ground. We use the ground data during this period of time to compare and verify the ground black carbon data measured by AE-33. Supplementary Figure S1 shows the comparison of ground black carbon concentration observed by AE-33 and AE-51 black carbon measuring instruments. The results show that, the correlation coefficient of the black carbon mass concentration data after correction by the two instruments reached 0.92, the value difference was small, and the change trend was the same. Therefore, it is believed that the observation results of AE-33 and AE-51 in this observation test are consistent.

SUPPLEMENTARY FIGURE S2
Comparison of ground black carbon concentration observations between AE-33 and AE-51 black carbon measuring instruments.

SUPPLEMENTARY FIGURE S3
Schematic diagram of the evolution of the boundary layer (Stull, 1988).

SUPPLEMENTARY FIGURE S4
Average virtual potential temperature profile of a typical profile (Stull, 1988). Stull R. B. An introduction to boundary layer meteorology. Klumer Academic Publishers, Dordretch, 665pp, 1988.

SUPPLEMENTARY FIGURE S5
Changes of surface pollutants and meteorological parameters over time from 1 January to 4, 2017 Relative humidity, precipitation, temperature **(B)** BC aerosol, wind direction, wind speed.

SUPPLEMENTARY FIGURE S6
Backward trajectory diagram of 00:00 on 2 January forward 24 h.

References

Altstdter, B., Deetz, K., Vogel, B., Babi, K., Lohou, F., Pacifico, F., et al. (2020). The vertical variability of black carbon observed in the atmospheric boundary layer during dacciwa. *Atmos. Chem. Phys.* 20 (13), 7911–7928. doi:10.5194/acp-20-7911-2020

Caputi, D. J., Faloona, I., Trousdell, J., Smoot, J., and Conley, S. (2018). Residual layer ozone, mixing, and the nocturnal jet in California's San Joaquin Valley. *Atmos. Chem. Phys.* 19, 4721–4740. doi:10.5194/acp-2018-854

Cass, G. R., Boone, P. M., and Macias, E. S. (1982). *Emissions and air quality relation-ships for atmospheric carbon particles in los angeles*. New York: Wolff, 207–244. doi:10.1007/978-1-4684-4154-3_13

Cheng, D., Wu, C., Wu, D., Liu, J., and Tian, Z. (2018). Characteristics of black carbon aerosols in urban guangzhou: Influencing factors in dry and rainy seasons. *Acta Sci. Circumstantiae* 38 (6), 2223–2232. doi:10.13671/j.hjkxxb.2018.0010

Corrigan, C. E., Roberts, G. C., Ramana, M. V., Kim, D., and Ramanathan, V. (2008). Capturing vertical profiles of aerosols and black carbon over the Indian Ocean using autonomous unmanned aerial vehicles. *Atmos. Chem. Phys.* 7 (4), 737–747. doi:10.5194/acp-8-737-2008

Countess, R. J., Wolff, G. T., and Cadle, S. H. (1980). The denver winter aerosol: A comprehensive chemical characterization. *J. Air Pollut. Control Assoc.* 30 (11), 1194–1200. doi:10.1080/00022470.1980.10465167

Delong, Z., Xuexi, T., Yang, G., Qiang, Z., Haijun, T., Kai, B., et al. (2015). In-situ aircraft measurements of the vertical distribution of black carbon in the lower troposphere of beijing, China, in the spring and summer time. *Atmosphere* 6 (5), 713–731. doi:10.3390/atmos6050713

Ding, A. J., Huang, X., Nie, W., Sun, J. N., Kerminen, V., Petaja, T., et al. (2016a). Enhanced haze pollution by black carbon in megacities in China. *Geophys. Res. Lett.* 43 (6), 2873–2879. doi:10.1002/2016GL067745

Ding, A. J., Huang, X., Nie, W., Sun, J. N., Kerminen, V. M., Petäjä, T., et al. (2016b). Size-related physical properties of black carbon in the lower atmosphere over beijing and europe. *Environ. Sci. Technol.* 53 (19), 11112–11121. doi:10.1021/acs.est.9b03722

Duforêt, L., Frouin, R., and Dubuisson, P. (2007). Importance and estimation of aerosol vertical structure in satellite ocean-color remote sensing. *Appl. Opt.* 46 (7), 1107–1119. doi:10.1364/AO.46.001107

Gordon, H. R. (1997). Atmospheric correction of ocean color imagery in the Earth Observing System era. *J. Geophys. Res.* 102 (D14), 17081–17106. doi:10.1029/96JD02443

Guiqin, F. U., Zhang, X., You, F., Tian, Y., and Erjie, L. I. (2016). Effect of meteorological conditions on PM2.5 concentration in shijiazhuang of hebei. *J. Arid Meteorology* 34 (02), 349–355. doi:10.11755/j.issn.1006-7639(2016)-02-0349

Guo, J., Miao, Y., Zhang, Y., Liu, H., Li, Z., Zhang, W., et al. (2016). The climatology of planetary boundary layer height in China derived from radiosonde and reanalysis data. *Atmos. Chem. Phys.* 16 (20), 13309–13319. doi:10.5194/acp-16-13309-2016

Hagler, G. S. W., Yelverton, T. L. B., Vedantham, R., Hansen, A. D. A., and Turner, J. R. (2011). Post-processing method to reduce noise while preserving high time resolution in aethalometer real-time black carbon data. *Aerosol Air Qual. Res.* 11 (5), 539–546. doi:10.4209/aaqr.2011.05.0055

Herich, H., Hueglin, C., and Buchmann, B. (2011). A 2.5 year's source apportionment study of black carbon from wood burning and fossil fuel combustion at urban and rural sites in Switzerland. *Atmos. Meas. Tech.* 4 (7), 1409–1420. doi:10.5194/amt-4-1409-2011

Huang, X., Wang, Z., and Ding, A. (2018). Impact of aerosol-PBL interaction on haze pollution: Multiyear observational evidences in north China. *Geophys. Res. Lett.* 45 (16), 8596–8603. doi:10.1029/2018GL079239

Li, J., Fu, Q. Y., Huo, J. T., Wang, D. F., Yang, W., Bian, Q. G., et al. (2015). Tethered balloon-based black carbon profiles within the lower troposphere of Shanghai in the 2013 East China smog. *Atmos. Environ. X.* 123, 327–338. doi:10.1016/j.atmosenv.2015.08.096

Li, Z. K. (1985). *Principles and applications of air pollution Meteorology*. Beijing: Meteorological Press, 0195.

Liang, R., Deng, Z. Z., Xu, X. B., Yan, P., Lin, W. L., Wang, Y., et al. (2016). Vertical profiles of black carbon measured by a micro-aethalometer in summer in the North China Plain. *Atmos. Chem. Phys.* 16 (16), 10441–10454. doi:10.5194/acp-16-10441-2016

Liu, D., Zhao, D., Xie, Z., Yu, C., Ding, D., Tian, P., et al. (2019). Enhanced heating rate of black carbon above the planetary boundary layer over megacities in summertime. *Environ. Res. Lett.* 14 (12), 124003. doi:10.1088/1748-9326/ab4872

Liu, Y., Wang, S., Shang, K., Yang, D., and Bin, Q. I. (2002). Time-space changing character of low-level wind in lanzhou city and its correlation with air pollution. *Plateau Meteorol.* 21 (3), 322. doi:10.3321/j.issn:1000-0534.2002.03.015

Lu, Y., Wang, Q. G., and Zhang, Y. Y. (2015). Remediation of PAH-contaminated soil by the combination of tall fescue, arbuscular mycorrhizal fungus and epigeic earthworms. *J. Hazard. Mat.* 51 (3), 535–541. doi:10.1016/j.jhazmat.2014.07.021

Lu, Y., Zhu, B., Huang, Y., Shi, S., Wang, H., An, J., et al. (2019). Vertical distributions of black carbon aerosols over rural areas of the Yangtze River Delta in winter. *Sci. Total Environ.* 661 (APR.15), 1–9. doi:10.1016/j.scitotenv.2019.01.170

Luan, S., and Mao, J. (1987). Measurements of the absorption coefficient of atmospheric aerosols. *J. Meteorological Res.* 44 (3), 198–205.

Miao, Y., Liu, S., Sheng, L., and Huang, S. (2019). Influence of boundary layer structure and low-level jet on PM2.5 pollution in beijing: A case study. *Int. J. Environ. Res. Public Health* 16 (4), 616. doi:10.3390/ijerph16040616

Pakkanen, T. A., Kerminen, V. M., Ojanen, C. H., Hillamo, R. E., Aarnio, P., and Koskentalo, T. (2000). Atmospheric black carbon in Helsinki. *Atmos. Environ. X.* 34 (9), 1497–1506. doi:10.1016/S1352-2310(99)00344-1

Petj, T., Jrvi, L., Kerminen, V. M., Ding, A. J., Kulmala, M., Nie, W., et al. (2016). Enhanced air pollution via aerosol-boundary layer feedback in China. *Sci. Rep.* 6, 18998. doi:10.1038/srep18998

Ramanathan, V., and Carmichael, G. (2008). Global and regional climate changes due to black carbon. *Nat. Geosci.* 36 (4), 221–227. doi:10.1038/ngeo156

Ramanathan, V., Crutzen, P. J., Kiehl, J. T., and Rosenfeld, D. (2002). Aerosols, climate, and the hydrological cycle. *Science* 294 (5549), 2119–2124. doi:10.1126/science.1064034

Raunemaa, T., Kikas, U., and Bernotas, T. (1994). Observation of submicron aerosol, black carbon and visibility degradation in remote area at temperature range

from 24 to 20°C. *Atmos. Environ. X.* 28 (5), 865–871. doi:10.1016/1352-2310(94)90245-3

Ren, Z., Zhang, Z., Sun, C., Liu, Y., Jun, L. I., Xiaohui, J. U., et al. (2015). Development of three-step quality control system of real-time observation data from aws in China. *Meteorol. Mon.* 41 (10), 1268–1277. doi:10.7519/j.issn.1000-0526.2015.10.010

Seidel, D. J., Zhang, Y., Beljaars, A., Golaz, J. C., Jacobson, A. R., and Medeiros, B. (2012). Climatology of the planetary boundary layer over the continental United States and Europe. *J. Geophys. Res.* 117 (D17). doi:10.1029/2012JD018143

Shi, S., Zhu, B., Lu, W., Yan, S., Liu, C., Liu, X., et al. (2020). Estimation of radiative forcing and heating rate based on vertical observation of black carbon in Nanjing, China. *Sci. Total Environ.* 756, 144135. doi:10.1016/j.scitotenv.2020.144135

Singh, V., Ravindra, K., Sahu, L., and Sokhi, R. (2018). Trends of atmospheric black carbon concentration over the United Kingdom. *Atmos. Environ. X.* 178 (APR), 148–157. doi:10.1016/j.atmosenv.2018.01.030

Slater, J., Coe, H., Mcfiggans, G., Tonttila, J., and Romakkaniemi, S. (2021). The effect of black carbon on aerosol-boundary layer feedback: Potential implications for Beijing haze episodes. *Atmos. Chem. Phys.* 22, 2937–2953. doi:10.5194/acp-2021-139

Stull, R. B. (1988). *An introduction to boundary layer Meteorology*. Netherlands: Springer. doi:10.1007/978-94-009-3027-8

Sun, Z. B., Liao, X. N., Wang, Z. S., Li, Z. M., and Hua, C. (2016) Scavenging effect of rime and east wind on PM2.5 under air heavy pollution in beijing. *Huan jing ke xue= Huanjing kexue/[bian ji, Zhongguo ke xue yuan huan jing ke xue wei yuan hui "Huan jing ke xue" bian ji wei yuan hui.]* 37 (10), 3679–3685. doi:10.13227/j.hjkx.2016.10.001

Tang, J., Wen, Y. P., Zhou, L. X., and Ling, X. (1999). Observational study of black carbon in clean air area of Western China. *Q. J. Appl. Meteorology* 10 (2), 160–170. doi:10.3969/j.issn.1001-7313.1999.02.004

Tian, P., Liu, D., Huang, M., Liu, Q., Zhao, D., Ran, L., et al. (2019). The evolution of an aerosol event observed from aircraft in Beijing: An insight into regional pollution transport. *Atmos. Environ. X.* 206, 11–20. doi:10.1016/j.atmosenv.2019.02.005

Tian, W., Chen, C., Huang, J., and Zhang, L. (1997). The solar heating effect of the winter aerosol in LaZhou and its influence on evolution of the mixed layer. *Q. J. Appl. Meteorology* 8 (3), 292–301. doi:10.1007/s00376-997-0061-6

Virkkula, A., Maekelae, T., Hillamo, R., Yli-Tuomi, T., Hirsikko, A., HaemeriKoponen, K. I. K., et al. (2007). A simple procedure for correcting loading effects of aethalometer data. *J. air & waste Manag. Assoc.* 57 (10), 1214–1222. doi:10.3155/1047-3289.57.10.1214

Vogelezang, D. H. P., and Holtslag, A. A. M. (1996). Evaluation and model impacts of alternative boundary-layer height formulations. *Bound. Layer. Meteorol.* 81 (3-4), 245–269. doi:10.1007/BF02430331

Waggoner, A. P., and Charlson, R. J. (1976). *Measurements of aerosol optical parameters*. Cambridge, Massachusetts: Academic Press, 511–533. doi:10.1016/B978-0-12-452950-2.50027-0

Wang, K. H., Shen, L., and Zhao, R. D. (2020). Anthropogenie ammonia emission invertory and its spatial distribution in Anhui Province from 2006 to 2017. *Trans. Atmos. Sci.* 43 (03), 547–556. doi:10.13878/j.cnki.dqkxxb.20191109006

Wang, X. Q., Yang, T., and Wang, Z. F. (2001). Impact of dust-haze episode from one air pollution control region to the other-one case study. *Clim. Environ. Res.* 16 (6), 690–696. doi:10.3878/j.issn.1006-9585.2011.06.02

Wang, Y. S. (1987). *Atmospheric physics [M]*. Beijing: Meteorological Press, 6–29.

Wang, Y., Vogel, J. M., Lin, Y., Pan, B., Zhang, R., Liu, Y., et al. (2018a). Aerosol microphysical and radiative effects on continental cloud ensembles. *Adv. Atmos. Sci.* 35 (2), 234–247. doi:10.1007/s00376-017-7091-5

Wang, Z., Huang, X., and Ding, A. (2018b). Dome effect of black carbon and its key influencing factors: Aone-dimensional modelling study. *Phys. Chem. A* 18, 1–29. doi:10.5194/acp-2017-967

Wei, W., Zhang, H., Cai, X., Song, Y., Zhang, H., Xiao, K., et al. (2020). Influence of intermittent turbulence on air pollution and its dispersion in winter 2016/2017 over beijing, China. *J. Meteorol. Res.* 34 (1), 176–188. doi:10.1007/s13351-020-9128-4

Weng, Y. P., Xu, X. B., Tang, J., Zhang, X. C., and Zhao, Y. C. (2001). Enrichment characteristics and origin of atmospheric aerosol elements at mt. *WaLiGuan. Q. J. Appl. Meteorology* 12 (4), 400–408. doi:10.3969/j.issn.1001-7313.2001.04.003

Wolff, G. T., Groblicki, P. J., Cadle, S. H., and Countess, R. J. (1982). *Particulate carbon at various locations in the United States*. US: Springer, 297–315. doi:10.1007/978-1-4684-4154-3_17

Xiao, X. Z., Liu, P. F., Geng, F. H., Gao, W., and Zhao, C. S. (2011). Comparison of black carbon aerosols in urban and suburban areas of Shanghai. *Q. J. Appl. Meteorology* 22 (2), 158–168. doi:10.3969/j.issn.1001-7313.2011.02.005

Yang, Y., Wang, L., Yong, H., Shi, C., and Tao, S. (2017). Impact of urbanization on meteorological observation and its environment representativeness: A case study of shouxian national climate station. *Ann. N. Y. Acad. Sci.* 45 (1), 7–14. doi:10.1111/nyas.13558

Zhang, D., Chen, B., Yamada, M., Niu, H., Wang, B., Iwasaka, Y., et al. (2012). Elevated soot layer in polluted urban atmosphere: A case study in beijing. *J. Meteorological Soc. Jpn.* 90 (3), 361–375. doi:10.2151/jmsj.2012-302

Zhang, R. J., Shi, L., and Liu, Y. (2007). High resolution observation and source identification of carbonaceous aerosols in PM10 in beijing in winter. *China Powder Sci. Technol.* 13 (6), 1–4. doi:10.3969/j.issn.1008-5548.2007.06.001

Zhang, X., Tang, J., Yunfei, W. U., Jian, W. U., Yan, P., and Zhang, R. (2015). Variations of black carbon aerosol observed in beijing and surrounding area during 2006—2012. *China Powder Sci. Technol.* 43, 6. doi:10.13732/j.issn.1008-5548.2015.04.006

Zhao, D., Huang, M., Tian, P., He, H., Lowe, D., Zhou, W., et al. (2019). Vertical characteristics of black carbon physical properties over Beijing region in warm and cold seasons. *Atmos. Environ. X.* 213, 296–310. doi:10.1016/j.atmosenv.2019.06.007

Zhao, D., Liu, D., Yu, C., Tian, P., Hu, D., Zhou, W., et al. (2020). Vertical evolution of black carbon characteristics and heating rate during a haze event in Beijing winter. *Sci. Total Environ.* 709, 136251. doi:10.1016/j.scitotenv.2019.136251